A bio-inspired origami capacitive robotic e-skin with multimodal sensing capabilities - Supplementary Information

Qian Xu[1], Boyang Zhang[1], Yik Kin Cheung[1], Zhiwei Yang[2], Rui Jiao[1], Shuhuai Yao[1], Wei Hong[2,*], and Hongyu Yu[3,*]

[1]The Hong Kong University of Science and Technology, Department of Mechanical and Aerospace Engineering, Hong Kong, 999077, China
[2]Southern University of Science and Technology, Department of Mechanics and Aerospace Engineering, Shenzhen, 518055, China
[3]The Hong Kong Polytechnic University, Department of Mechanical Engineering, Hong Kong, 999077, China
[*]Corresponding author. Email: hongw@sustech.edu.cn (W.H.); hongyu.yu@polyu.edu.hk (H.Y.)

The PDF file includes:

Note S1. Super-resolution Theory.
Note S2. Origami Based Super-resolution.
Note S3. Miura-ori geometry Analysis.
Note S4. Multi-layer Design with Crease Optimizations.
Note S5. Curved Surface Tessellation.
Note S6. AD7147 Power-up and Register Writing&Reading.
Note S7. Comparison Between Three Different Algorithms.
Note S8. Multi-point Touch Realization Analysis.

Figure S1. Definitions of super-resolution.
Figure S2. Schematic of origami-based super-resolution tactile sensing.
Figure S3. Nature and theory of origami-based super-resolution.
Figure S4. Miura-ori pattern geometric parameter definitions.
Figure S5. Poisson's ratios for Miura-ori patterns.
Figure S6. Simulation verification of crease optimizations.
Figure S7. FEA results for different package designs under the same external load.
Figure S8. Stress distribution for different sizes of vertex cut.
Figure S9. Electric potential and electric field of shear force sensing layer.
Figure S10. Capacitance changes in origami-structured electrodes during unfolding.
Figure S11. Origami pattern curved surface tessellation.
Figure S12. Fabrication process.
Figure S13. E-skin coordinate and sensing unit definitions (top view).
Figure S14. E-skin test and machine learning data collection platform.
Figure S15. Repeatability: readout of S1 when a 1N load was applied in cell (2,1) for 10000 times.
Figure S16. Repeatability test results of other cells.
Figure S17. Stability of the FPC design under different folding conditions.
Figure S18. Force-CDC output curve for different indenter size when load is applied in cell (4,3).

Figure S19. Performance of e-skin under different power supply and grounding conditions.
Figure S20. Performance of e-skin under different temperature (t) and humidity (RH) circumstances.
Figure S21. Typical application schematic of TCA9548A.
Figure S22. Performance comparison of CNNs, ResMLPs and MLPs.
Figure S23. Real-time localization and force estimation without prescribed CDC output threshold.
Figure S24. Performance comparison of different inputs (MLPs).
Figure S25. Robustness test of proposed e-skin.
Figure S26. Schematic of proposed e-skin under single external load.
Figure S27. Schematic of proposed e-skin under two external loads.
Figure S28. Generation of two-point touch training data
Figure S29. Schematic of tested 6 points for verifying the generated data for two-point touch.
Figure S30. Performance of two-non-adjacent-point touch.

Table S1. Comparison of generated data and collected data for two-point touch.

Other Supplementary Material for this manuscript includes the following:

Movie S1. Human-machine interaction demonstrations. (.mp4 format).

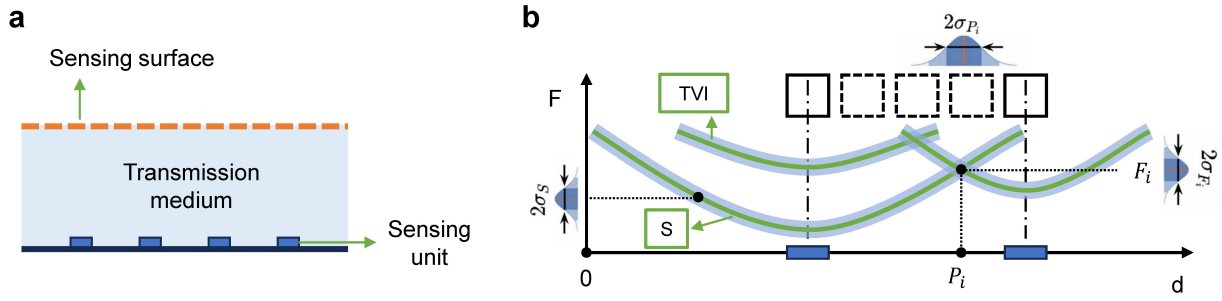


Figure S1. Definitions of super-resolution. (a) Schematic of tactile sensor array. (b) Schematic of the realization of super-resolution. The orange TVIs (taxel value isolines[1]) that are the force F needed to elicit the same taxel value S depending on the distance d from the sensor unit. The intersection of TVIs of two sensors indicates a hypothetical contact point Pi with a force strength F_i. The measurement noise σ_S in shaded blue leads to uncertainty of the position σ_{Pi} and force σ_{Fi}.

Note S1: Super-resolution Theory

Sensor arrays are widely employed in tactile sensing to achieve large-area coverage and high spatial resolution. Yet, as the array size increases, wiring complexity, circuit design, and signal processing pose increasing challenges. To address these limitations, researchers have developed various super-resolution strategies. Super-resolution refers to systems in which the tactile sensing resolution surpasses the physical density of sensing elements. It allows spatial perception beyond the spacing of individual taxels, analogous to the hyperacuity of human skin. This capability is essential for robotics, prosthetics, and human–machine interactions that require fine touch perception. By combining advanced transduction mechanisms and computational methods, super-resolution reduces wiring complexity, manufacturing costs, and fragility while improving spatial accuracy.

The schematic and definition of super-resolution are shown in Figure S1. A traditional tactile sensor is constructed from a sensing surface (contact surface), a transmission medium (e.g., an elastomer), and some taxel/sensing units. Virtual contacts can also be regarded as part of their structure in terms of the minimum distance at which external forces can be localized within their working range, as shown in Figure S1(a).

For traditional tactile sensors, under the application of a single external load, the sensor's output signals depend on both the magnitude of the applied load and the distance between the force application point and the sensing points. In addition, measurement noise is present across different sensing units. Therefore, to localize the external load, TVI (Taxel Value Isoline)[1] was introduced, as indicated by the orange lines in Figure S1(b) (curve S). TVI indicates the magnitude of the external load required at different positions to achieve the same outputs at the sensing points. For each S-curve in Figure S1(b), it represents a combination of external load magnitude and position that can produce the same output signal at the sensing unit. From the figure, it is also evident that the farther from the sensing unit, the greater the external load required to achieve the same output.

As shown in Figure S1(b), when an external load causes changes in the output signals at both sensing units, the corresponding S-curves (TVI) for the outputs of these two sensing units can be plotted. The intersection point of these two curves, with a horizontal coordinate d and a vertical coordinate F, represents the position and magnitude of the external load. Therefore, the external load can be localized and its magnitude estimated.

Therefore, based on previous analyzes, the super-resolution factor[1] for the 2D case is defined as:

$$\Omega = \frac{D}{n \cdot 2\sigma_P} \tag{1}$$

where D is the distance between two sensing units, n is the number of sensing units, and σ_P is the spatial resolution (or localization error) of the tactile sensor. For the calculation of the super-resolution factor for the 2D case, the following equation can also be utilized:

$$\Omega = \frac{Area}{n * \pi * RMSE_x * RMSE_y} \tag{2}$$

where $Area$ is the overall sensing area, n is the total number of sensing units, $RMSE_x$ and $RMSE_y$ are the root mean square errors in the x and y directions.

The fundamental principle behind super-resolution lies in changes in the signal output caused by the deformation and subsequent transmission through the medium. As shown in Figure S1(b), external load can only be localized when the S-curves of the two sensing units overlap. Therefore, in this study, whether the tactile sensor is super-resolution is defined as follows: For the 1D case, if twice the localization error $2\sigma_P$ is smaller than the distance between two sensing units D, it is considered super-resolution; otherwise, it is not. For the 2D case, if the product of the localization errors in the x and y directions is less than the sensing area assigned to each sensing unit, which is $RMSE_x * RMSE_y$ smaller than $\frac{Area}{n}$, it is considered super-resolution; otherwise, it is not.

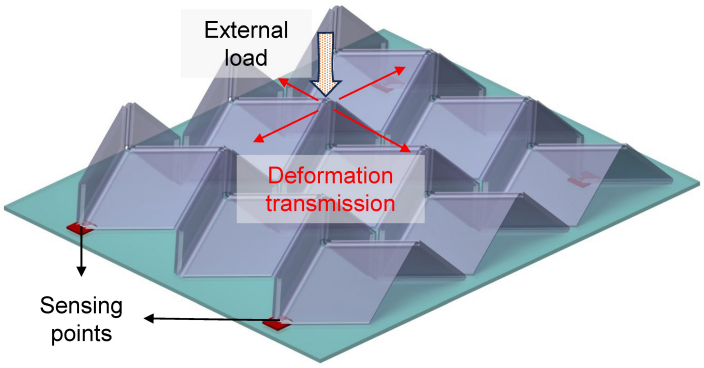


Figure S2. Schematic of origami-based super-resolution tactile sensing. When external load is applied, the origami cell will deform in the loaded area, and the deformation will be propagated according to the nature of origami structure. By measuring the displacements of specific locations, the location and magnitude of external load can be estimated.

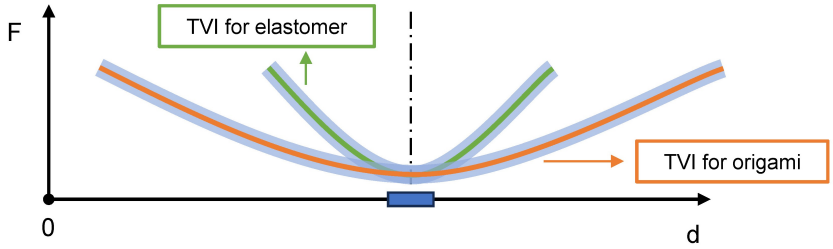


Figure S3. Nature and theory of origami-based super-resolution. Based on the deformation transmission capability, the TVI curve will become flatter.

Note S2: Origami Based Super-resolution

The schematic origami-based super-resolution is shown in Figure S2. According to Figure S2, when an external load is applied to the origami structure, the part under load will deform. Because of the folding and unfolding properties of this structure, the deformation of the part under load will be transmitted in different directions. Therefore, the spacing between sensing points can be much larger than traditional sensor arrays. By measuring displacements at specific locations, the location and magnitude of the external load can be estimated from the displacement relationships.

The principles of Origami-based super-resolution are shown in Figure S3. From the previous analysis, we know that the position and magnitude of an external load can only be calculated when the S-curves of two sensing units intersect. If the two S-curves do not intersect, localizing the external load requires either increasing its magnitude or reducing the distance between the sensing units. However, the amplitude of the external load cannot be infinite; it is subject to limitations, or the sensor's structural integrity could be compromised. Reducing the distance between sensing units, however, brings us back to the issues of sensor arrays. However, with the use of the Origami structure as the transmission medium, due to its deformation transmission capability, the TVI curves will become flatter, as shown in Figure S3. Therefore, under the external load amplitude limitation, even with a larger distance between the two sensing units, the intersection of the two S curves can still be achieved, indicating that a large super-resolution factor can be realized by leveraging the origami structure.

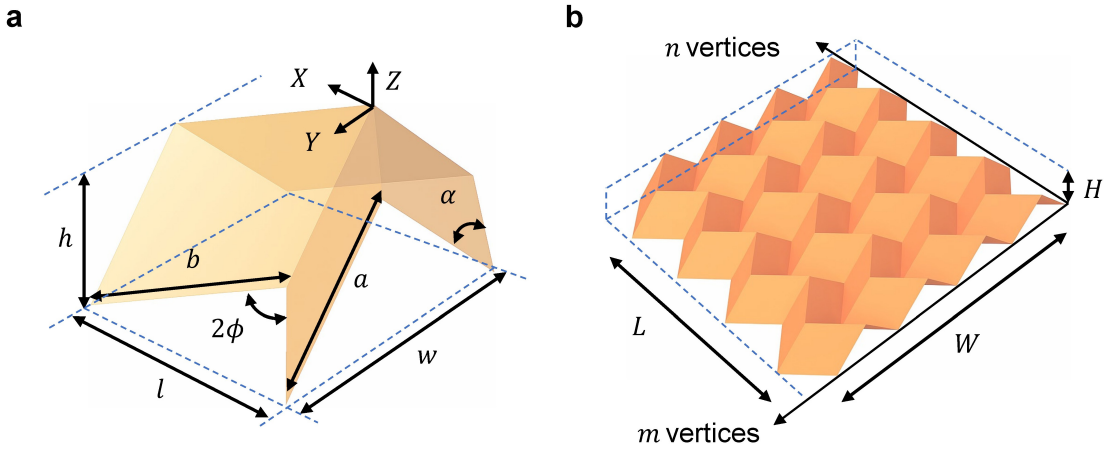


Figure S4. Miura-ori pattern geometric parameter definitions. (a) Single cell. (b) Multiple cells (global scenario).

Note S3: Miura-ori Geometry Analysis

The Miura-ori geometric definitions are shown in Figure S4, with the single cell provided again for clarity (Figure S4a). For a unit cell, the geometric relations are:

$$\begin{aligned} l &= 2b\sin\phi \\ w &= 2a\cos\alpha\sec\phi \\ h &= a\sqrt{\sin^2\alpha-\sin^2\phi}\sec\phi \end{aligned} \tag{3}$$

For the global structure, the Miura-ori pattern can be enclosed in a rectangular frame of length L, width W, and height H (Figure S4b). Since L and W are typically much larger than H, they are defined as in-plane, with H as out-of-plane. The overall dimensions of an ideal rigid Miura-ori structure are:

$$\begin{aligned} L &= (n-1)b\sin\phi \\ W &= (m-1)a\cos\alpha\sec\phi + b\cos\phi \\ H &= a\sqrt{\sin^2\alpha-\sin^2\phi}\sec\phi \end{aligned} \tag{4}$$

Here, n and m denote the number of vertices along L and W, respectively. The extra term $b\cos\phi$ in W reflects the tail effect, where the structure's total width is not simply the sum of unit cell widths w. This effect is significant for small m, influencing folding behavior and necessitating kinematic analysis at the full-structure level. Considering Equation (4), the in-plane Poisson's ratio of the Miura-ori structure is:

$$\nu_{12} = -\frac{\frac{dL}{L}}{\frac{dW}{W}} = -\frac{dL}{dW}\frac{W}{L} = -\cot^2\phi\,\frac{a\cos\alpha\cdot(m-1)/b+\cos^2\phi}{a\cos\alpha\cdot(m-1)/b-\cos^2\phi} \tag{5}$$

According to Equation (5), the in-plane Poisson's ratio ν_{12} depends on both the folding angle ϕ and the geometric term $a\cos\alpha\cdot(m-1)/b$. Figure S5a illustrates this dependence, showing that ν_{12} can be

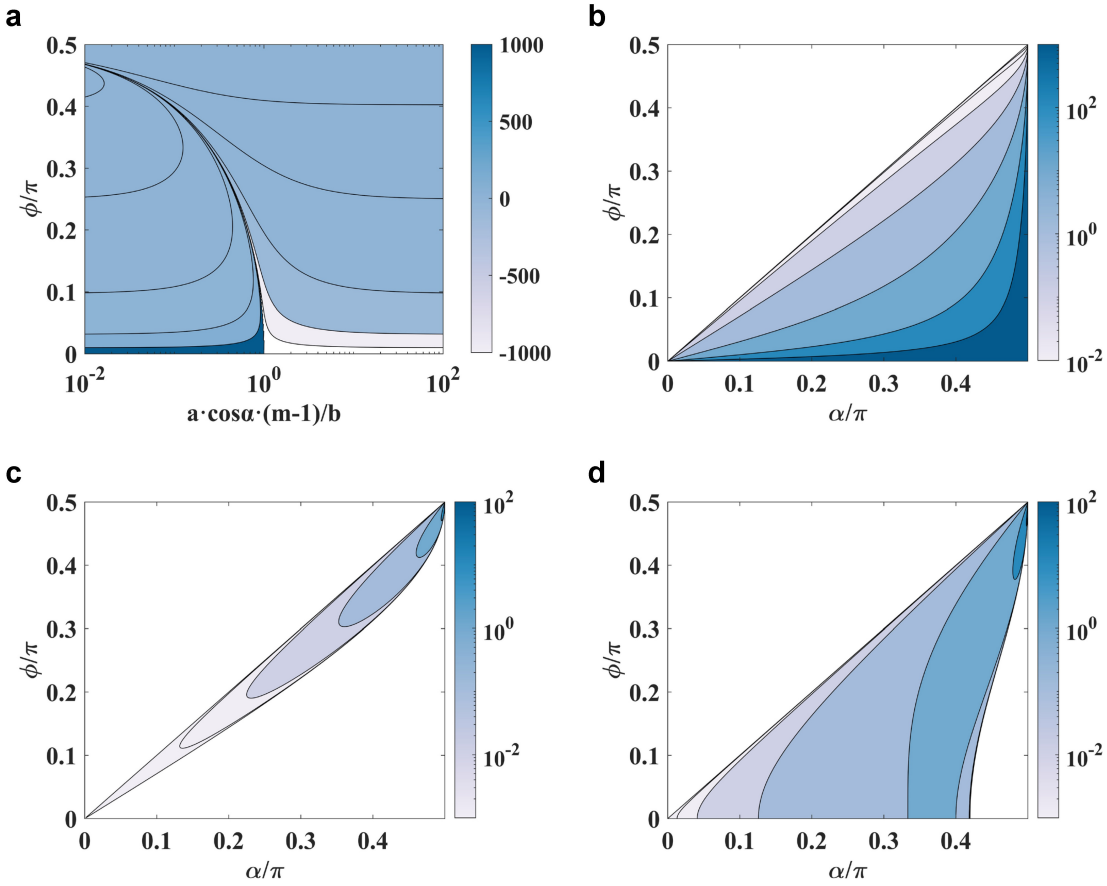


Figure S5. Poisson's ratios for Miura-ori patterns. (a) In-plane Poisson's ratio ν_{12} for different values of $a \cdot \cos\alpha \cdot (m-1)/b$ and ϕ. (b) Out-of-plane Poisson's ratio ν_{13}. (c) Out-of-plane Poisson's ratio ν_{23} when $a(m-1)/b = 1$. (d) Out-of-plane Poisson's ratio ν_{23} when $a(m-1)/b = 4$.

positive or negative depending on geometry and folding. The transition boundary is clearly defined, with ν_{12} diverging when the denominator in Equation (5) approaches zero. Near this singularity, a small load in the W direction induces disproportionately large deformation in L, which may benefit precision sensing.

When $\nu_{12} = 0$, loading along W causes no deformation along L, enabling directional decoupling useful for vibration isolation and impact protection. For large m, edge effects are negligible, and ν_{12} can be approximated by a single cell:

$$\widetilde{\nu_{12}} = -\frac{\frac{dl}{l}}{\frac{dw}{w}} = -\frac{dl}{dw}\frac{w}{l} = -\cot^2\phi \tag{6}$$

Here, w and l denote single-cell width and length (Figure S4a). Under this simplification, ν_{12} is always negative for $\phi \leq \alpha$ and increases monotonically with ϕ. The complementary ν_{21} is the reciprocal of ν_{12}.

The out-of-plane Poisson's ratios are:

$$\nu_{13} = -\frac{\frac{dL}{L}}{\frac{dH}{H}} = -\frac{dL}{dH}\frac{H}{L} = \cot^2\phi\frac{\sin^2\alpha - \sin^2\phi}{\cos^2\alpha} \tag{7}$$

$$\nu_{23} = -\frac{\frac{dW}{W}}{\frac{dH}{H}} = -\frac{dW}{dH}\frac{H}{W} = \frac{(\sin^2\alpha - \sin^2\phi)[a\cos\alpha\cdot(m-1)/b - \cos^2\phi]}{\cos^2\alpha[a\cos\alpha\cdot(m-1)/b + \cos^2\phi]} \tag{8}$$

Figures S5b–d show their dependence on geometry and folding. ν_{13} is always positive since $\phi \leq \alpha$, and increases as folding progresses. ν_{23}, however, can be positive or negative. As $a(m-1)/b$ increases, the negative region diminishes; beyond a critical threshold, ν_{23} remains positive for all α within design limits.

For robotic skin, maintaining positive ν_{13} and ν_{23} simplifies load transmission and enhances sensing reliability. With large m, tail effects vanish, giving constant ν_{23} and a simplified ν_{13}:

$$\widetilde{\nu_{13}} = -\frac{\frac{dl}{l}}{\frac{dh}{h}} = -\frac{dl}{dh}\frac{h}{l} = \frac{\sin^2\alpha - \sin^2\phi}{\cos^2\alpha} \tag{9}$$

which is always positive.

This analysis guides origami-based tactile design. Adequate sensitivity requires sufficiently large ν_{13} and ν_{23} to ensure effective force transmission. For uniform deformation in both X and Y, the design condition $\nu_{13} = \nu_{23}$ yields $\phi = \pi/4$. Panel lengths were set to $a = b = 10,\text{mm}$, and $\alpha = 50^\circ$ were selected to balance Poisson's ratios, thickness, and sensitivity.

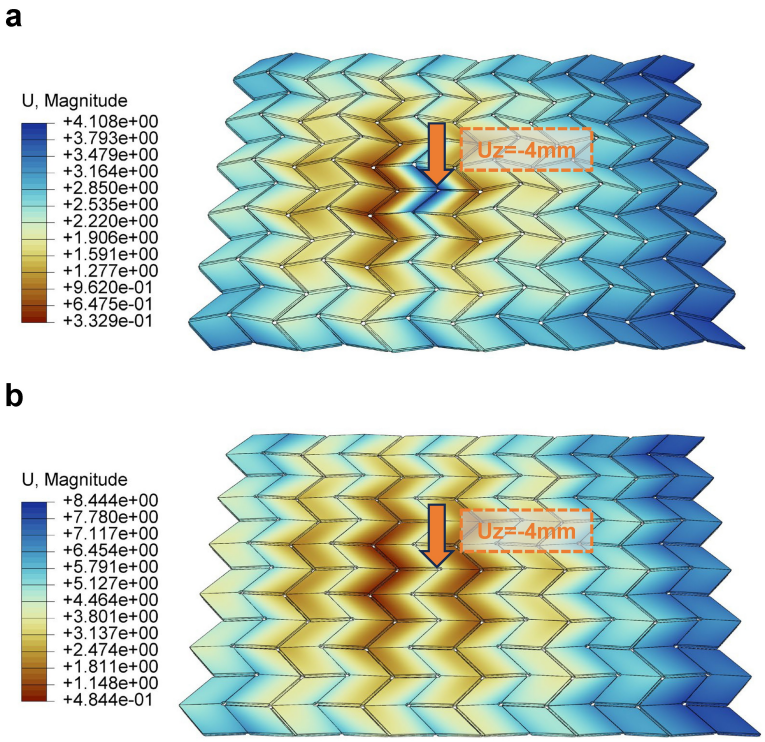


Figure S6. Simulation verification of crease optimizations. (a) Final displacement field of multi-layer Origami without crease optimizations. (b) Final displacement field of multi-layer Origami with crease optimizations.

Note S4: Multi-layer Design with Crease Optimizations

To evaluate the effect of multi-layer crease optimization (narrowed mountain creases and released valley creases in upper stiffeners, with the opposite in lower stiffeners), finite element analysis was performed (Figure S6). Figure S6a shows the initial state and boundary conditions: all bottom vertices were constrained in the Z direction, and a vertical displacement of -4mm was applied to the top vertex of the center cell to drive unfolding. Displacement fields without and with crease optimization are presented in S6b and c, respectively.

Without optimization (S6b), deformation was concentrated in the center, with limited propagation. With optimization (S6c), deformation propagated globally, approaching a rigid-foldable state.

Narrowing mountain creases and releasing valley creases markedly improves rigid-foldability but constrains folding to a single direction, where mountain and valley folds are uniquely determined. While this restricts some applications, it does not hinder functionality for large-area e-skin.

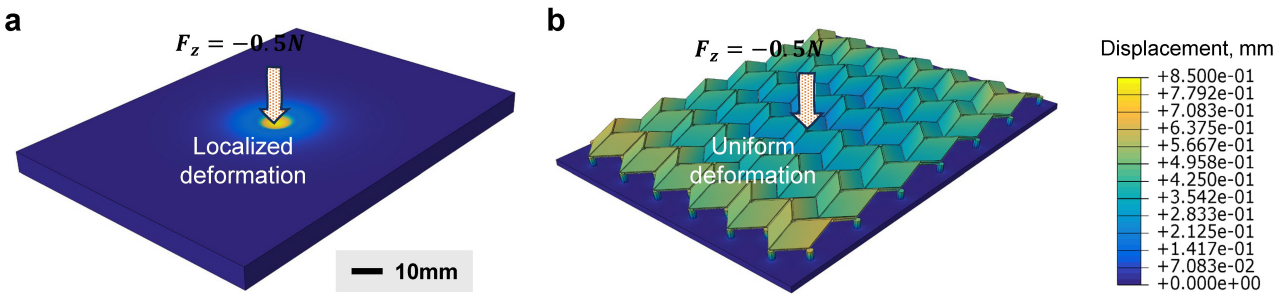


Figure S7. FEA results for different package designs under the same external load. (a) Elastomer cube (Ecoflex-0030), (b) Pillar array design. Under the same external load, the maximum of elastomer cube is large. However, the deformation only happens in a quite narrow range, making it unsuitable for large area tactile sensing. For our proposed origami with pillar array design, under the same external load, deformation can propagate for a quite long distance; when external load disappears, the pillar array will bring origami structure back to the initial state. This shows the feasibility of origami structure to be used for larger area, super-resolution tactile skin. Note: Since elastomer cannot transmit deformation over a long distance, the spacing between sensing points cannot be made very large. Although machine learning can still achieve a good SR factor, most practical applications do not require such high precision (0.1mm level). Furthermore, with this design, wiring complexity increases significantly as the area grows. These issues can be solved by using origami structures.

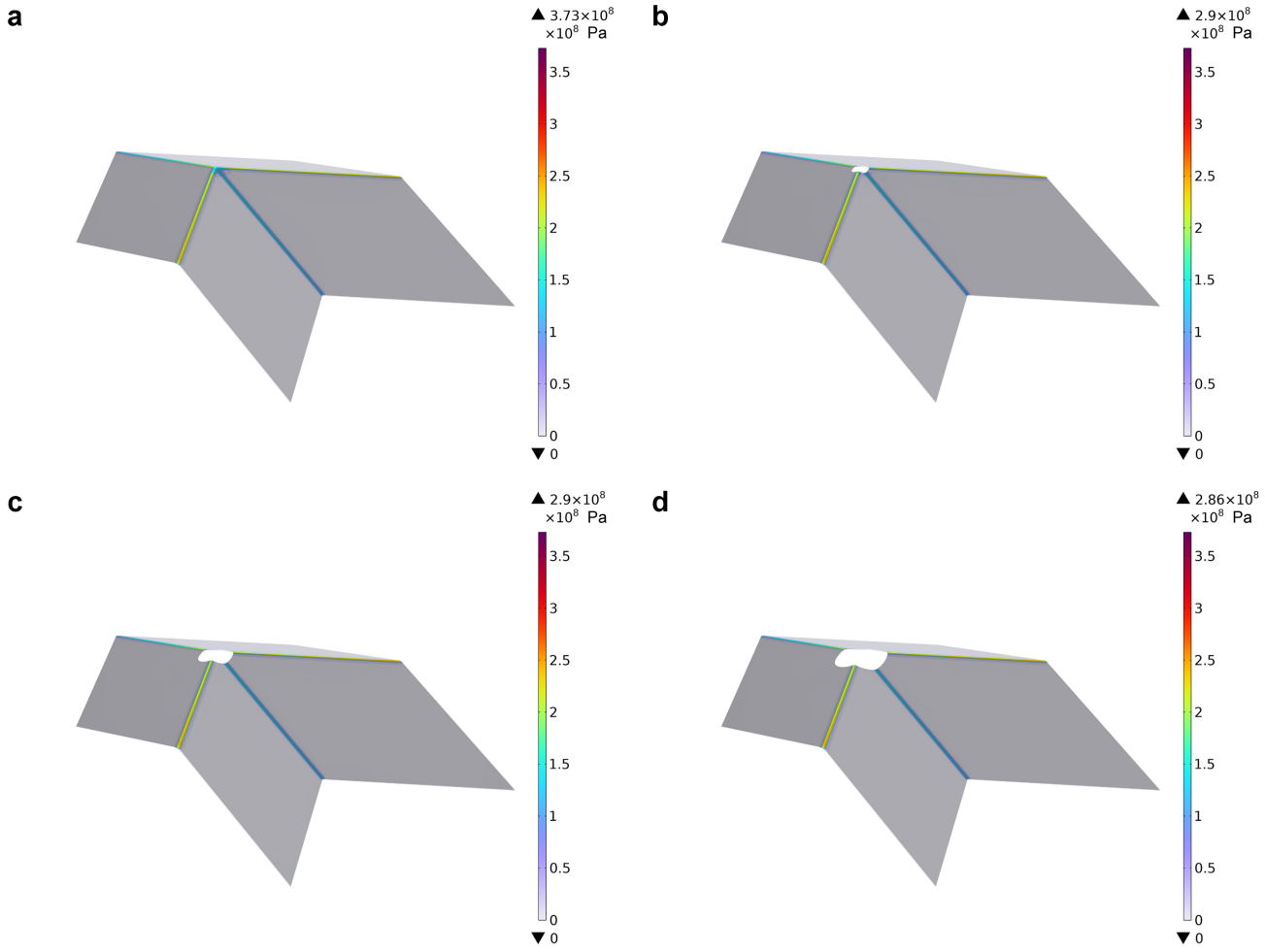


Figure S8. Stress distribution for different sizes of vertex cut. (a) Without vertex cut. (b) Circular cut with radius of 0.5 mm. (c) Circular cut with radius of 1 mm. (d) Circular cut with radius of 1.5 mm. Vertex cut optimization markedly reduces stress concentration. The maximum stresses for 0.5mm and 1mm cuts are nearly identical, and further increasing the cut size yields diminishing reductions. However, excessively large cuts reduce available area for electronic components. In different applications, the size of vertex cut can be determined by the stress analysis and also electronic component configuration requirements.

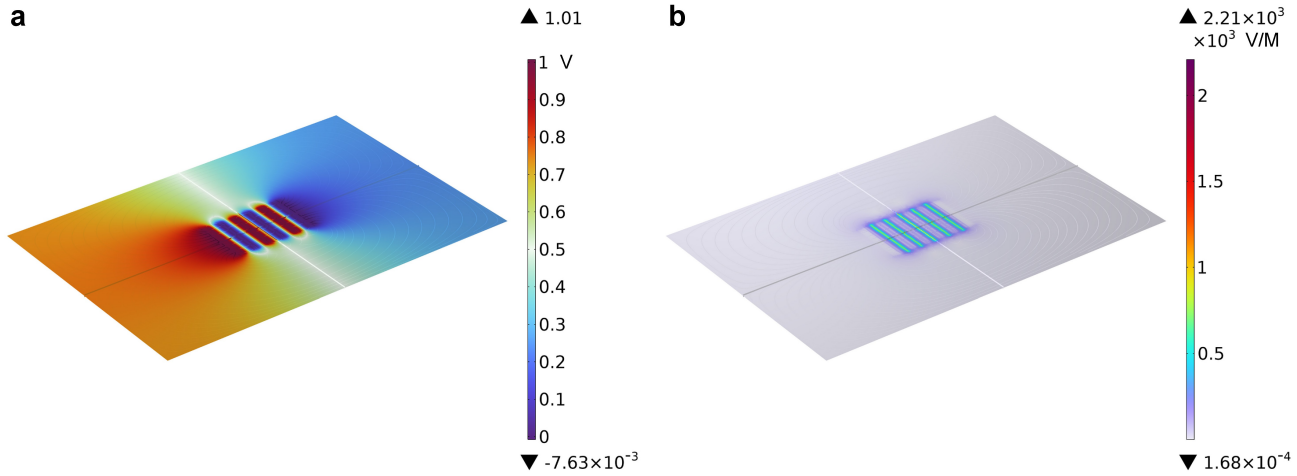


Figure S9. Electric potential and electric field of shear force sensing interdigital electrodes under a shear force of 1 N. (a) Electric potential when under a shear load of 1N along the direction perpendicular to electrode length direction. (b) Electric field of the electrodes under the same load and boundary conditions of (a). The shear-sensing layer comprises two interdigital electrode sections, oriented along the X and Y axes, respectively. According to the design parameters, a gap W exists between the upper and lower electrodes; therefore, the disturbance from normal load when measuring shear force can be significantly eliminated.

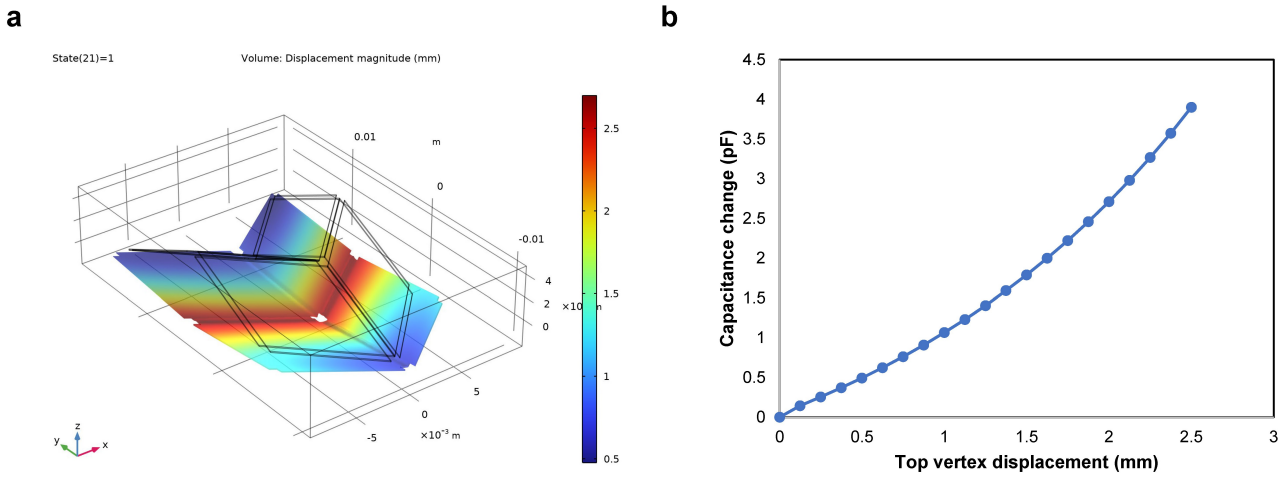


Figure S10. Capacitance changes in origami-structured electrodes during unfolding. (a) Initial state of the structure (dashed outline) and unfolded state. (b) Relationship between top vertex displacement and capacitance change. It can be observed that as displacement increases, the capacitance change rate increases (meaning greater capacitance change per unit displacement) because of the expand of origami structure. This relationship, combined with the structural stiffness characteristics, results in the linearity of the F-CDC curve (Figures 4c and d).

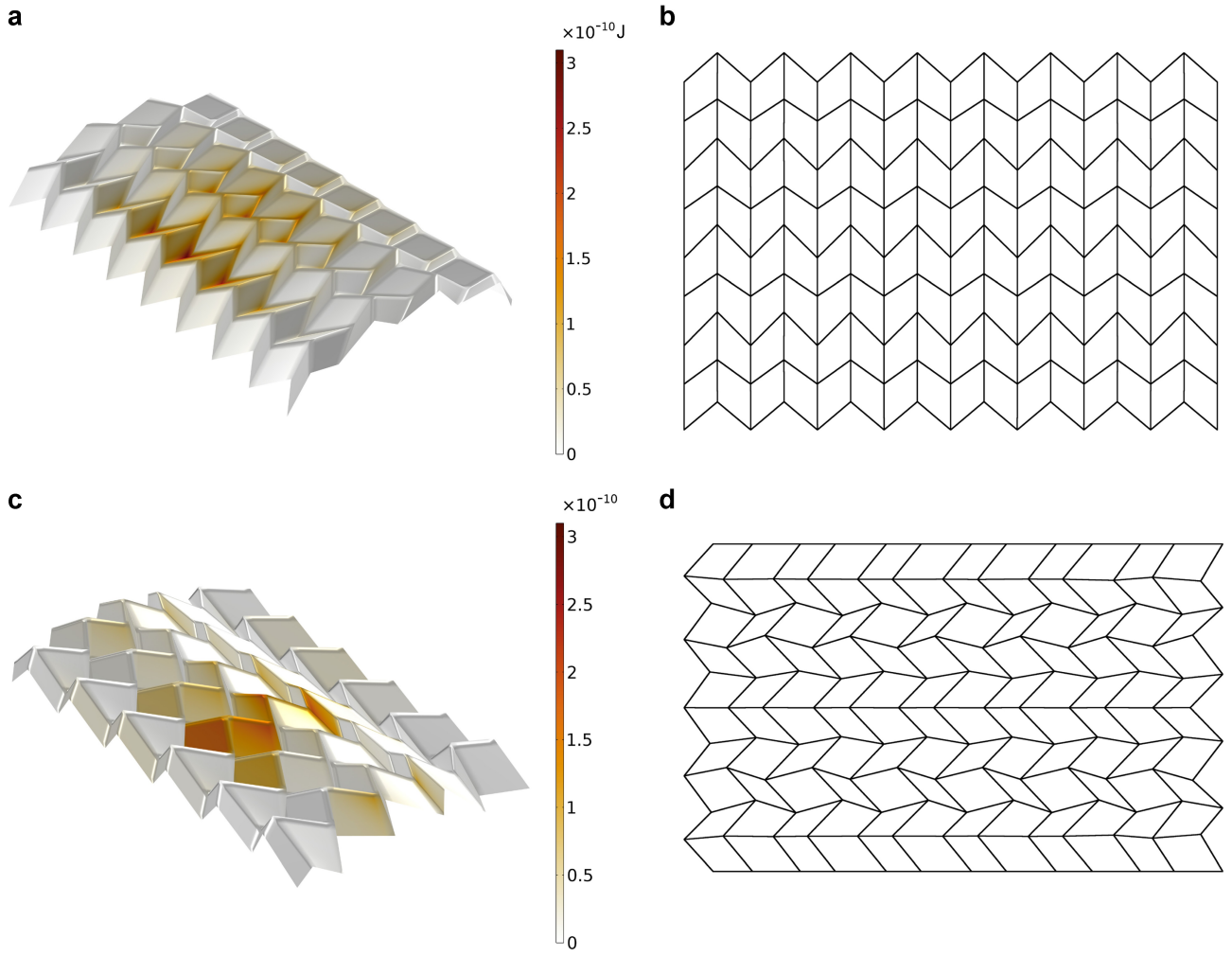


Figure S11. Origami pattern curved surface tessellation. (a) Elastic energy distribution when optimizing along W direction. (b) Optimized 2D pattern when optimizing along W direction. (c) Elastic energy distribution when optimizing along L direction. (d) Optimized 2D pattern when optimizing along L direction.

Note S5: Curved Surface Tessellation

Origami structures can conform to curved surfaces, but bending a planar sheet for attachment introduces residual stress, impairing foldability. Thus, an appropriate tessellation algorithm is required[2–4]. Here, a previously developed algorithm[5] was used to design curved patterns by minimizing the total strain energy during attachment. For clarity, the optimization process is restated.

The in-plane stretching energy is given by[6]:

$$W_{stretching} = C_1(I_1 - 3) \tag{10}$$

where C_1 is half the initial shear modulus, and $I_1 = \lambda_1^2 + \lambda_2^2 + \lambda_3^2 = \mathrm{tr}(\mathbf{C}) = C_{II}$ is the first invariant of the right Cauchy-Green tensor. The out-of-plane bending stiffness is expressed as[7]:

$$W_{bending} = B(k_1^2 + k_2^2) = B \cdot b_{\alpha\beta} b_{\alpha\beta} \tag{11}$$

where k_1 and k_2 are the principal curvatures. Then the total elastic energy of the Origami structure is[5]:

$$W[\mathbf{x}(\mathbf{X})] = \int_A \left[\tau(C_{II} + \frac{1}{\det(\mathbf{C})} - 3) + b_{\alpha\beta} b_{\alpha\beta} \right] dA \tag{12}$$

where τ adjusts the relative contributions of stretching and bending. The tessellation problem is thus a nested minimization:

$$\min_{\mathbf{X}(\mathbf{X_0})} \left(\min_{\mathbf{x}(\mathbf{X})} W[\mathbf{x}(\mathbf{X}(\mathbf{X}_0))] \right) \tag{13}$$

Where $\mathbf{x}(\mathbf{X})$ is the attaching process, and $\mathbf{X}(\mathbf{X_0})$ is the in-plane folding process. Panel size and geometry can be tuned via coefficients; damping factors may be introduced to enhance convergence and suppress excessive distortion.

Two tessellation orientations were tested along the L and W directions (Figure S4). For a cylindrical surface of $100,\text{mm}$ diameter, elastic energy distributions and corresponding 2D patterns are shown in Figures S11a–d. Tessellation along W minimized size variation and preserved panel morphology, whereas tessellation along L slightly reduced peak strain energy but introduced large distortions in panel size and shape. These deviations affect both the mechanical behavior and the integration of electronic components. Therefore, tessellation along the W direction was selected.

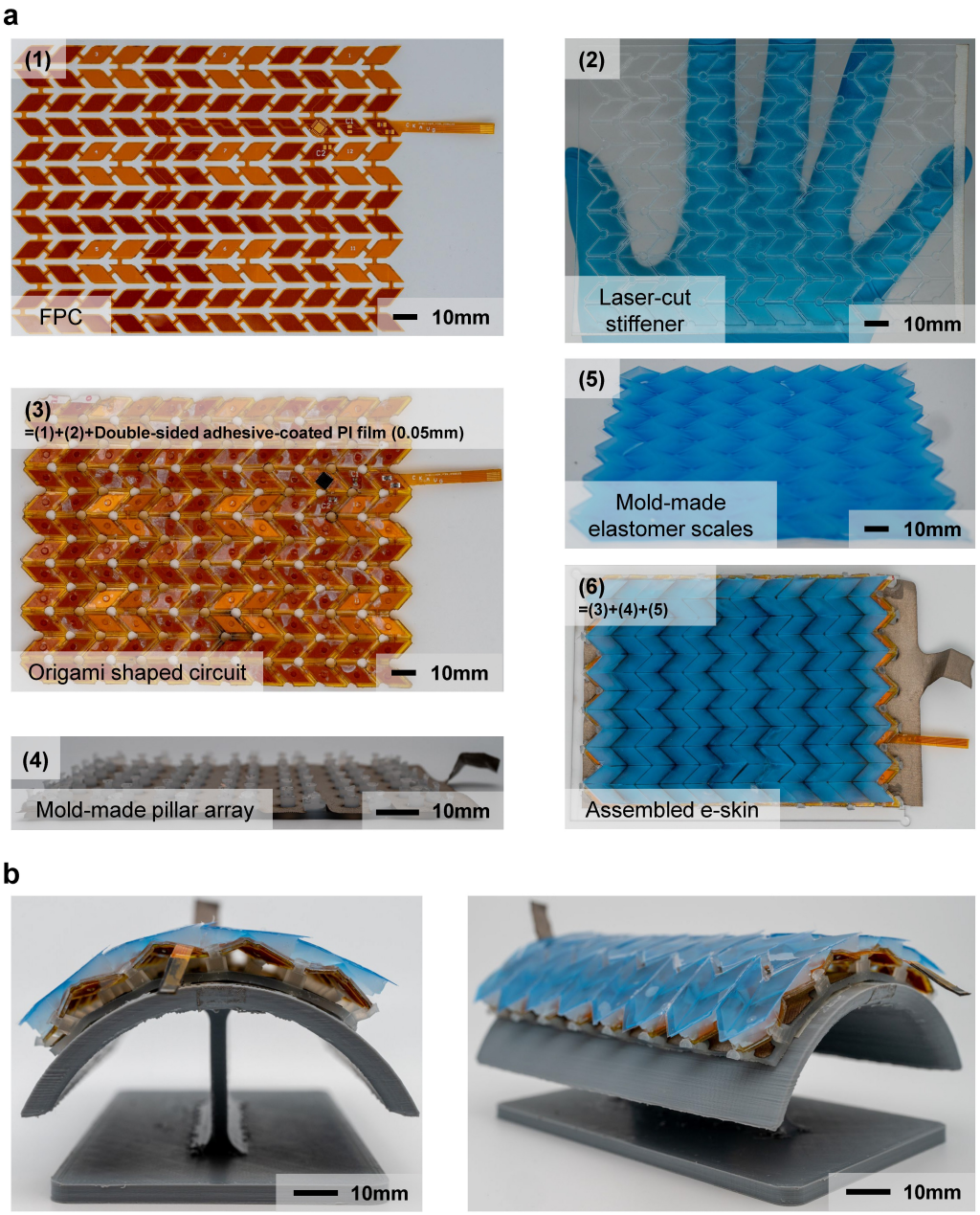


Figure S12. Fabrication process. (a) The fabrication process of planar e-skin. (1) The FPC was designed, fabricated, and populated with electronic components. (2) Upper and lower stiffeners with designed patterns (0.5 mm acrylic) were laser cut. (3) The FPC was combined with the double-layer stiffeners to form the multilayer Origami circuit. (4) A pillar array was molded from Ecoflex-0030, and a laser-cut conductive tape pattern was attached as the ground electrode. (5) Elastomer scales of Ecoflex-0030 were molded, with a PI film coated in aluminum added as the proximity sensing layer. (6) The shear sensing layer was also molded. Finally, the Origami circuit, pillar array, and elastomer scales were assembled into the complete e-skin. (b) Photos of curved e-skin, which has the same fabrication process as the planar counterparts.

Note S6: AD7147 Power-up and Register Writing&Reading

The AD7147 chip requires register read/write operations to configure its functions before use. The power-up sequence is:

1. Turn on the power supplies to the chip.

2. Write to the Bank 2 registers at Address 0x080 through Address 0x0DF. (Note that the Bank 2 register values are unique for each application. Register values come from characterization of the sensor in the application).

   In our proposed e-skin application (Figure 3b), the 9 electrodes (planar case) are connected with CIN1-CIN7, CIN11 and CIN12, and their signals were stored in stage 1 - stage 9, respectively. CIN0 and stage 0 are used for proximity sensing, while CIN 8, CIN9 and stage 10, satge 11 are used for shear force sensing. Take CIN1 as an example: the signal from CIN1 is stored in stage 1, and CIN1 is connected to the CDC positive input, therefore '0X80' (hexadecimal, 000000000001000 in binary) is written to address '0X88'. Following the same process, the offset, sensitivity, and all the relevant settings can be prescribed according to the application requirements. For the e-skin, the settings for stage 1 and CIN 1 are as follows:

```
    uint16_t stage1_data1 = 0x08;
    writeReg(STAGE1_CONNECTION, &stage1_data1, 2);
    uint16_t stage1_data2 = 0x00;
    writeReg(STAGE1_CONNECTION+1, &stage1_data2, 2);
    uint16_t STAGE1_AFE_OFFSET_data = 0x800;  // Offset
    writeReg(STAGE1_CONNECTION+2, &STAGE1_AFE_OFFSET_data, 2);
    uint16_t STAGE1_SENSITIVITY_data = 0x00;
    writeReg(STAGE1_CONNECTION+3, &STAGE1_SENSITIVITY_data, 2);
    uint16_t STAGE1_OFFSET_LOW_data = 0x00;
    writeReg(STAGE1_CONNECTION+4, &STAGE1_OFFSET_LOW_data, 2);
    uint16_t STAGE1_OFFSET_HIGH_data = 0x00;
    writeReg(STAGE1_CONNECTION+5, &STAGE1_OFFSET_HIGH_data, 2);
    uint16_t STAGE1_OFFSET_HIGH_CLAMP_data = 0x00;
    writeReg(STAGE1_CONNECTION+6, &
       STAGE1_OFFSET_HIGH_CLAMP_data, 2);
    uint16_t STAGE1_OFFSET_LOW_CLAMP_data = 0x00;
    writeReg(STAGE1_CONNECTION+7, &STAGE1_OFFSET_LOW_CLAMP_data
       , 2);
```

3. Write to the Bank 1 registers at Address 0x000 through Address 0x007. (Caution: At this time, Address 0x001 must remain set to a default value of 0x0000 during this contiguous write operation). Register values: Address 0x000 = 0x82B2; Address 0x001 = 0x000; Address 0x002 = 0x3230 (depends on number of conversion stages used); Address 0x003 = 0x419; Address 0x004 = 832; Address 0x005 = interrupt enable register (depends on required interrupt behavior); Address 0x006 = interrupt enable register (depends on required interrupt behavior); Address 0x007 = interrupt enable register (depends on required interrupt behavior).

   In the e-skin application, all the conversion stage will be utilized, therefore, the setting is:

```
    // Use all the conversion stages
    uint16_t PWR_CONTROL_full = 0x2B0;
    writeReg(PWR_CONTROL, &PWR_CONTROL_full, 2);
```

Then set the ambient compensation and interrupt after setting address 0x001 to a default value of 0x0000:

```
    // set address 0x001 to 0x0000
    uint16_t stageEnable1 = 0x0000;
    writeReg(STAGE_CAL_EN, &stageEnable1, 2);
    // Ambient compensation
    uint16_t AMB_COMP_CTRL0_data = 0xFF0;
    uint16_t AMB_COMP_CTRL1_data = 0x164;
    uint16_t AMB_COMP_CTRL2_data = 0xFFFF;
    writeReg(AMB_COMP_CTRL0, &AMB_COMP_CTRL0_data, 2);
    writeReg(AMB_COMP_CTRL1, &AMB_COMP_CTRL1_data, 2);
    writeReg(AMB_COMP_CTRL2, &AMB_COMP_CTRL2_data, 2);
    // Interrupt settings
    uint16_t STAGE_LOW_INT_EN_data = 0x0000;
    uint16_t STAGE_HIGH_INT_EN_data = 0x0000;
    uint16_t STAGE_COMPLETE_INT_EN_data = 0x0000;
    writeReg(STAGE_LOW_INT_EN, &STAGE_LOW_INT_EN_data, 2);
    writeReg(STAGE_HIGH_INT_EN, &STAGE_HIGH_INT_EN_data, 2);
    writeReg(STAGE_COMPLETE_INT_EN, &STAGE_HIGH_INT_EN_data, 2)
       ;
```

4. Write to the Bank 1 register, Address 0x001 = 0x0FFF (depends on number of conversion stages used). Here, all the conversion stages are used:

```
    uint16_t stageEnable2 = 0x03FF;
    writeReg(STAGE_CAL_EN, &stageEnable2, 2);
```

5. Read back the corresponding interrupt status register at Address 0x008, Address 0x009, or Address 0x00A.

6. Repeat Step 5 every time $\overline{\text{INT}}$ is asserted.

   In the tactile sensing application, interrupt is not required. When in working state, the e-skin will keep reading signals then estimate the magnitude and location of external load. Therefore, the interrupt related settings can be deployed as default:

```
    uint16_t interrupt_status_1 = 0;
    readReg(STAGE_LOW_LIMIT_INT, &interrupt_status_1, 2);
    uint16_t interrupt_status_2 = 0;
    readReg(STAGE_HIGH_LIMIT_INT, &interrupt_status_2, 2);
    uint16_t interrupt_status_3 = 0;
    readReg(STAGE_COMPLETE_LIMIT_INT, &interrupt_status_3, 2);
```

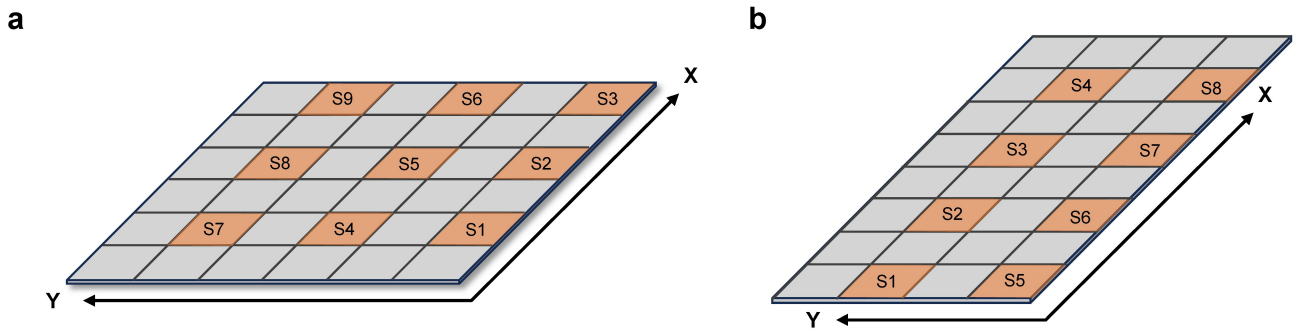


Figure S13. E-skin coordinate and sensing unit definitions (top view). (a) Planar configuration. There are 9 electrodes in total, with one cell left empty between each electrode in both the X and Y directions. (b) Curved configuration. There are 8 electrodes in total, with one cell left empty between each electrode in both the X and Y directions.

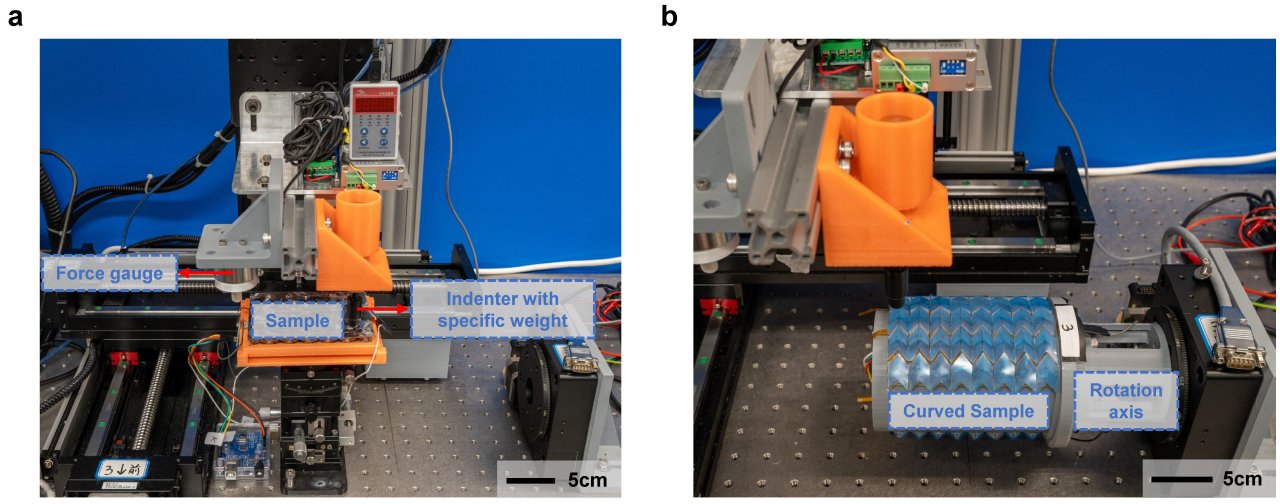


Figure S14. E-skin test and machine learning data collection platform. (a) Setup for planar configuration. (b) Setup for curved configuration. The normal force is adjusted by using different weights when collecting the machine learning training data; Force gauge is used when testing the characteristics. For planar configurations, the three motion axes X, Y, and Z are employed; for curved configurations, the Y-axis is replaced by the rotational axis R.

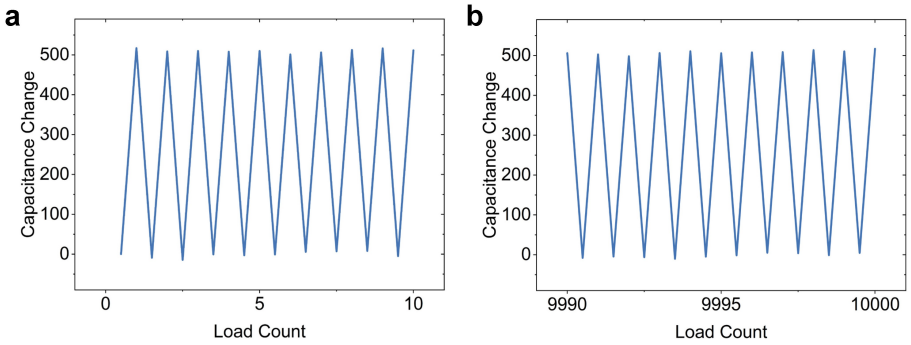


Figure S15. Repeatability test results: readout from S1 when a 1 N load was applied in cell (2,1) for 10000 times. (a) CDC output of first 10 cycles. (b) CDC output of last 10 cycles. No significant differences are observed for these 10 cycles, demonstrating the high repeatability of the proposed Origami e-skin.

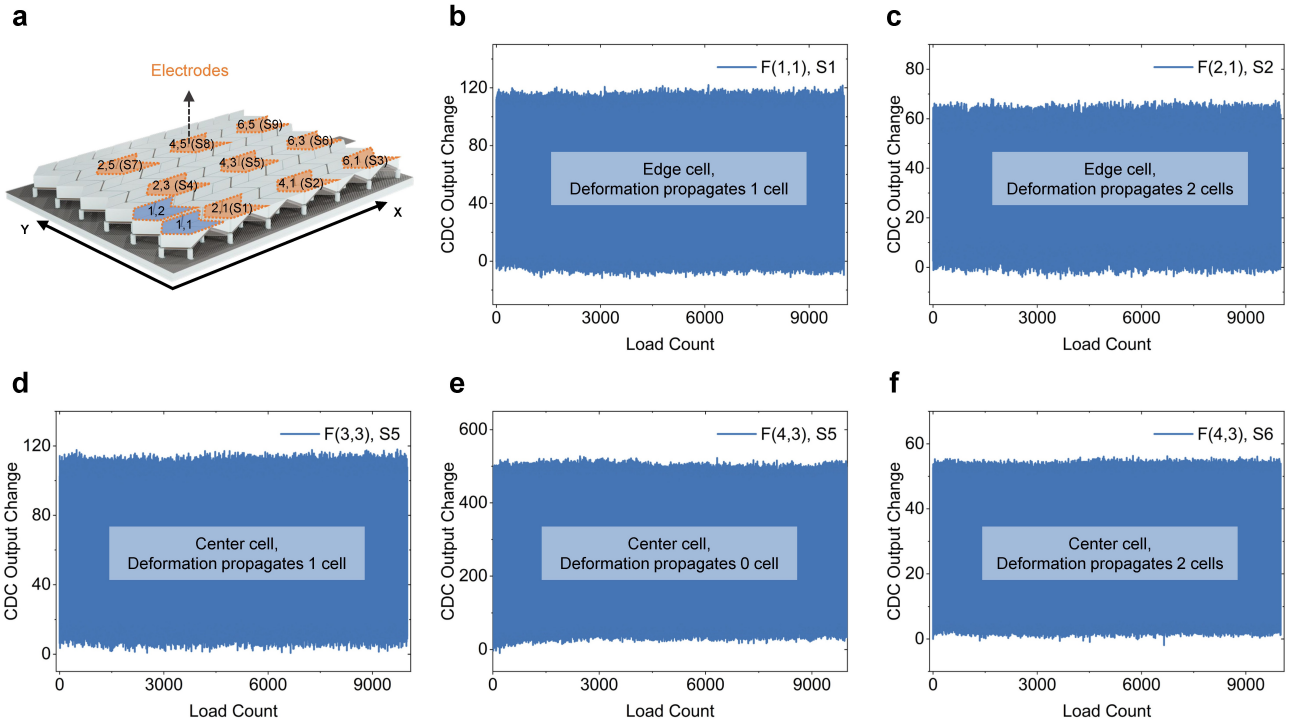


Figure S16. Repeatability test results of other cells. (a) Coordinate definitions, shown here again for convenience. (b) Readout from S1 when a 1 N load was applied in cell (1,1) for 10000 times. (c) Readout from S2 when a 1 N load was applied in cell (2,1) for 10000 times. (d) Readout from S5 when a 1 N load was applied in cell (3,3) for 10000 times. (e) Readout from S5 when a 1 N load was applied in cell (4,3) for 10000 times. (f) Readout from S6 when a 1 N load was applied in cell (4,3) for 10000 times. The results show good repeatability for both center and edge cells. Additionally, the repeatability does not affect by the deformation propagation over cells.

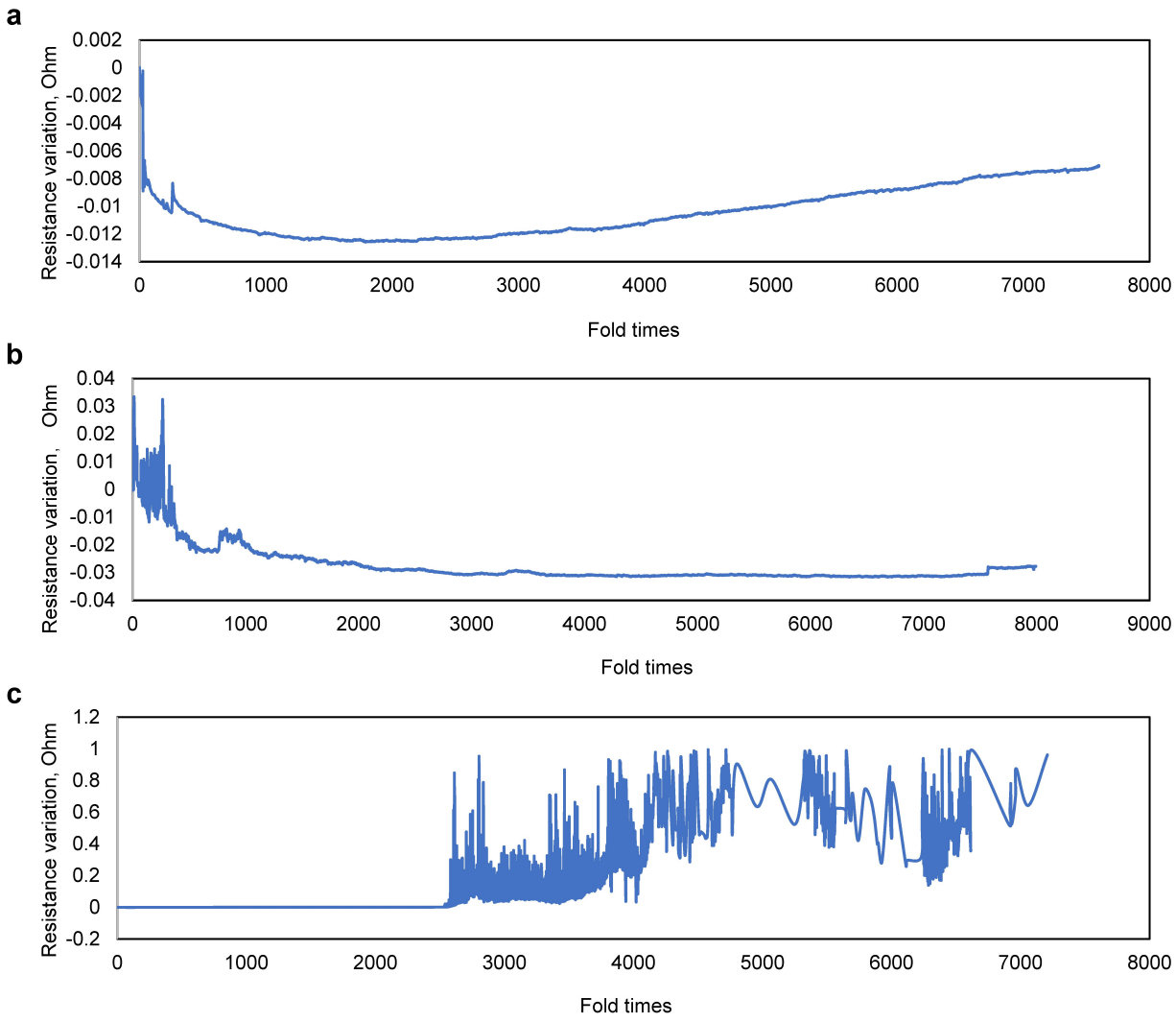


Figure S17. Stability of the FPC design under different folding conditions. Here, single cells from the FPC in Figure 3 are cut out and folded from 0 degrees to 90 degrees. The resistance of their internal traces is measured and recorded. (a) Resistance changes without pre-creasing and stiffeners. (b) Resistance changes with pre-creasing but without stiffeners. (c) Resistance changes with both pre-creasing and stiffeners. The results indicate that when both pre-creases and stiffeners are present, the resistance at the crease location undergoes significant changes after the FPC is folded from 0 to 90 degrees over 2,500 times. This suggests the possibility of fine cracks forming in the traces at the crease. However, in actual use, we do not incorporate pre-creases, and the bending angle of the FPC within the origami structure is small—typically not exceeding 30 degrees—thus ensuring its stability. Additionally, the bending stability of FPCs can be enhanced through fabrication processes (electrolytic copper vs. roll-formed copper) or by utilizing different materials (such as liquid metal).

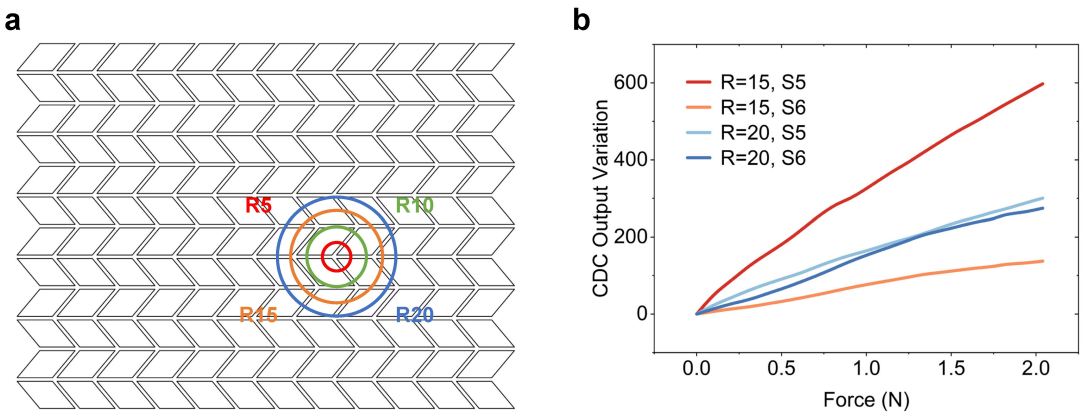


Figure S18. Force-CDC output curve for different indenter size when load is applied in cell (4,3). (a) Schematic of load application by different sized-indenters. (b) F-CDC output curve when using different indenters. When the indenter area increases, it simultaneously covers more than one cell. This causes multiple cells within the loaded region to deform concurrently, resulting in different signal outputs. If the indenter coverage remains confined to a single cell, the indenter size does not significantly affect the output curve due to the presence of the origami structure as a deformation carrier.

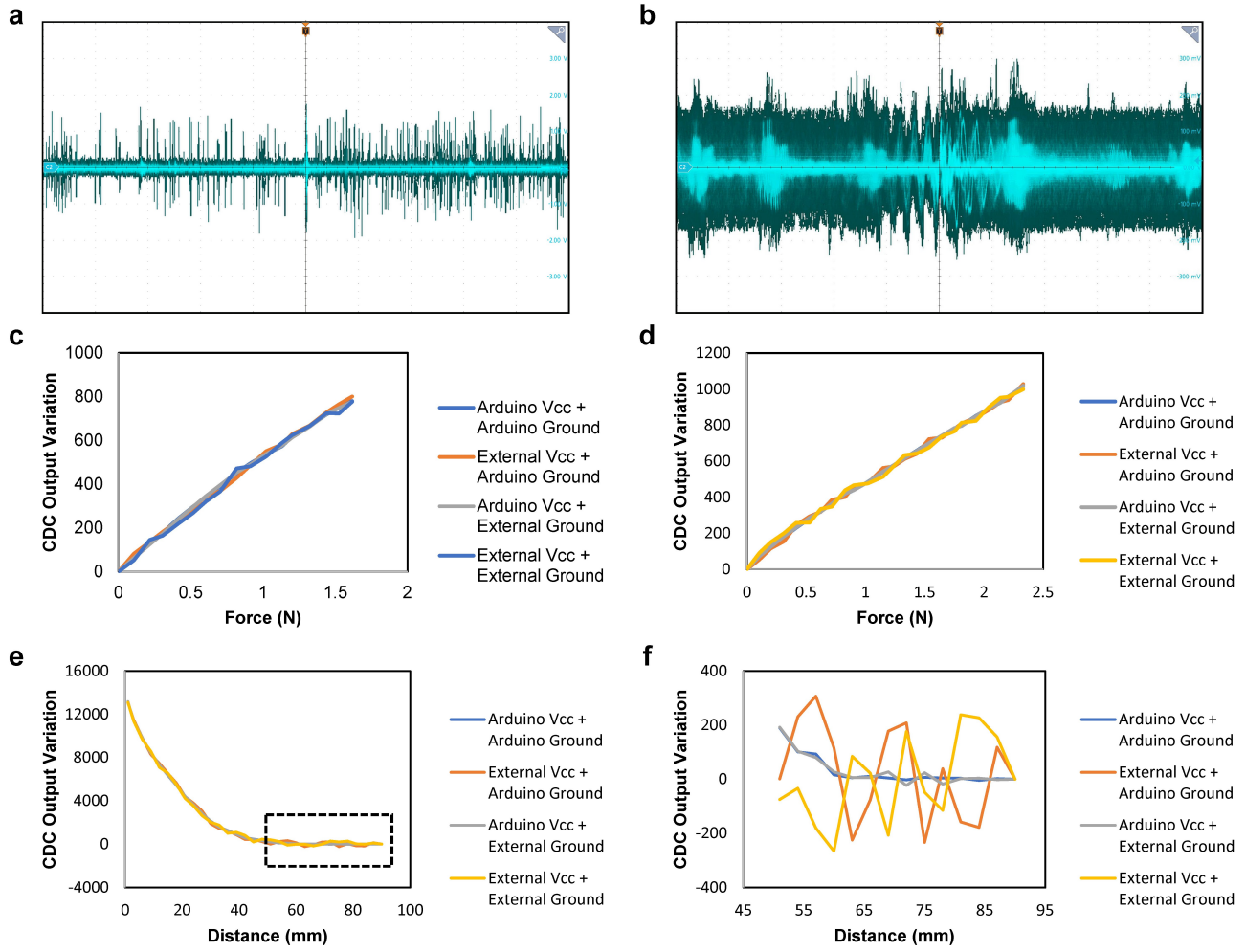


Figure S19. Performance of e-skin under different power supply and grounding conditions. (a) The waveform of the Arduino Uno's 3.3V power supply measured by the oscilloscope (Tektronix MDO34, TEKTRONIX, INC.). Peak-peak value: 40 mV, RMS: 8mV. (b) The waveform of the external power supply (MCH-K302D, MCH Instruments CO.,Ltd.) measured by the oscilloscope. Peak-peak value: 992 mV, RMS: 20mV. (c) F-CDC readout variation curve of S2 when load is applied on cell (2,1). (d) F-CDC readout variation curve of S5 when load is applied on cell (4,3). (e) Proximity sensing performance of a 70 mm × 90 mm conductive plate. (f) Zoom in of (e). The results demonstrate that different power supply conditions significantly impact the chip's performance. If necessary, a voltage regulator such as the TPS7A47 can be implemented to stabilize the input voltage.

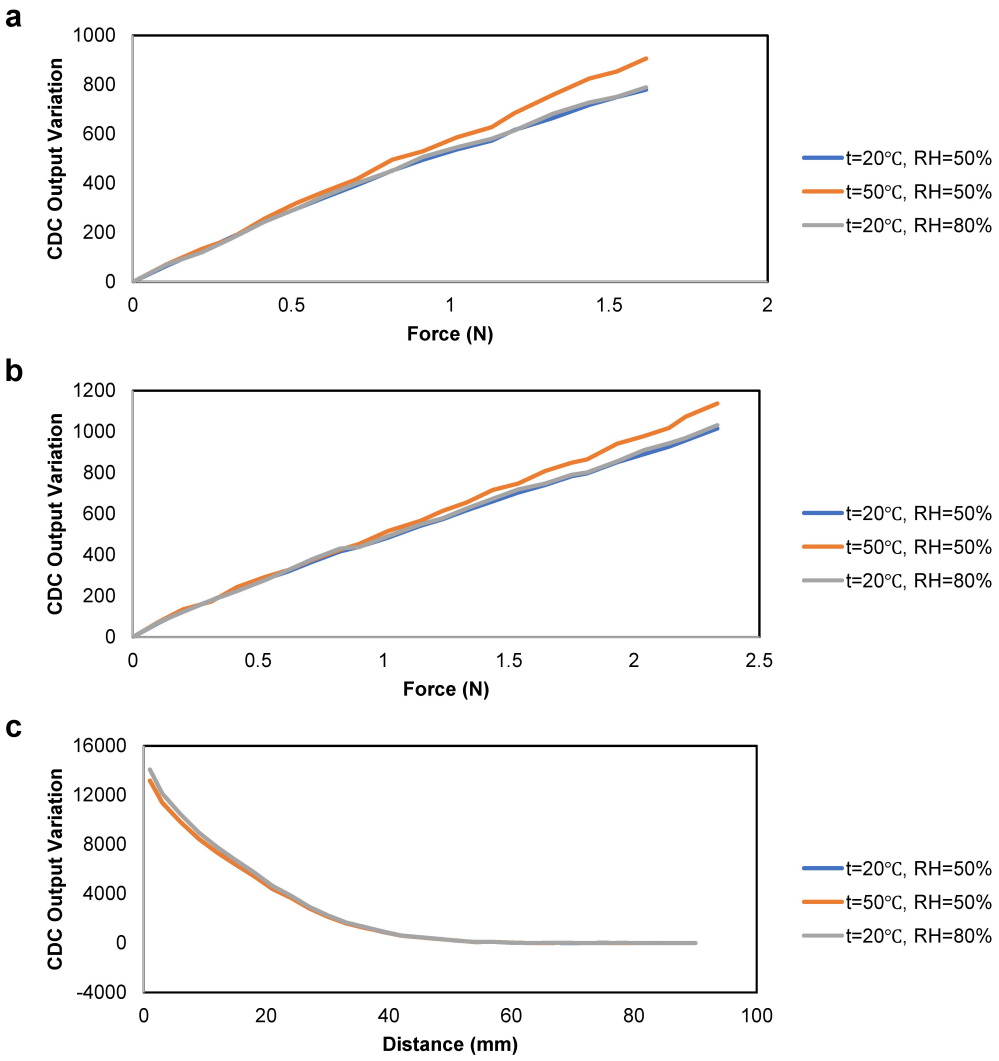


Figure S20. Performance of e-skin under different temperature (t) and humidity (RH) circumstances. (a) F-CDC readout variation curve of S2 when load is applied on cell (2,1) in different circumstances. (b) F-CDC readout variation curve of S5 when load is applied on cell (4,3) in different circumstances. (c) Proximity sensing performance of a 70 mm × 90 mm conductive plate under in different circumstances. The results indicate that humidity has no significant impact on the device's performance, as the AD7147 incorporates built-in environmental compensation. The effect of temperature on performance primarily arises from the decrease in the elastic modulus of the elastomer as temperature increases, leading to increased sensitivity.

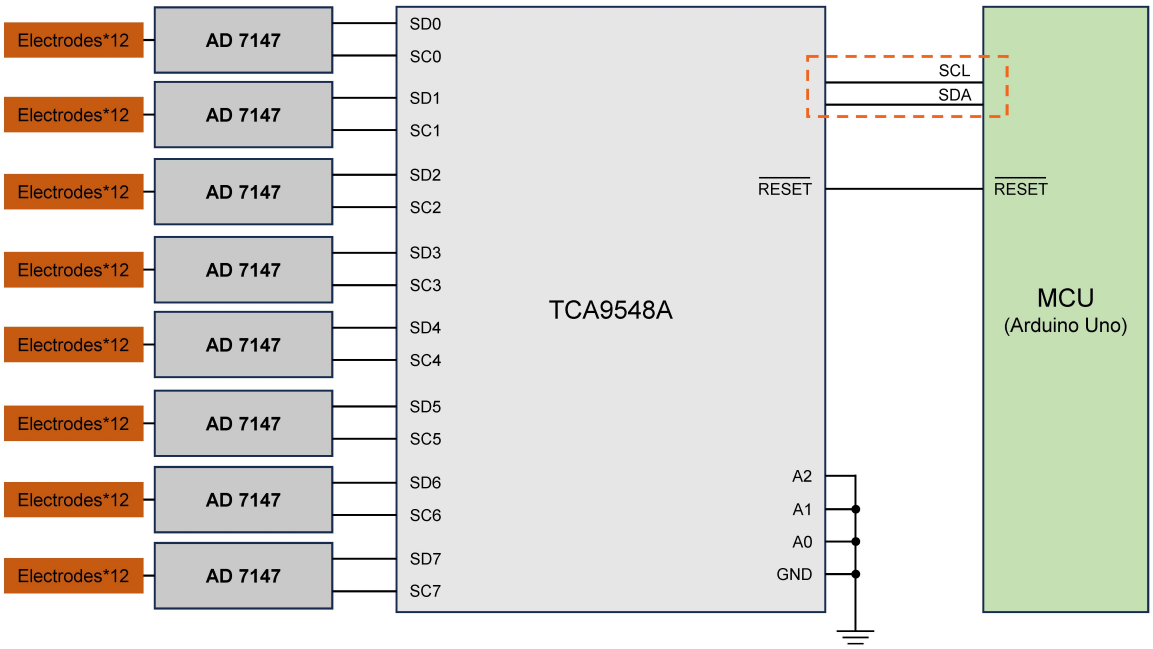


Figure S21. Typical application schematic of TCA9548A. The AD7147 can simultaneously read the capacitance of multiple electrodes (12 in our application), which is advantageous for large-area sensing. However, when the sensing area becomes very large, the limited number of input ports necessitates enlarging Origami cells, increasing thickness and potentially degrading localization and force estimation. To address this, the TCA9548A—a low-voltage 8-channel I^2C switch with reset capability—can expand the number of measurable inputs from 12 to 96, thereby greatly enhancing the scalability of the proposed e-skin for large-area applications.

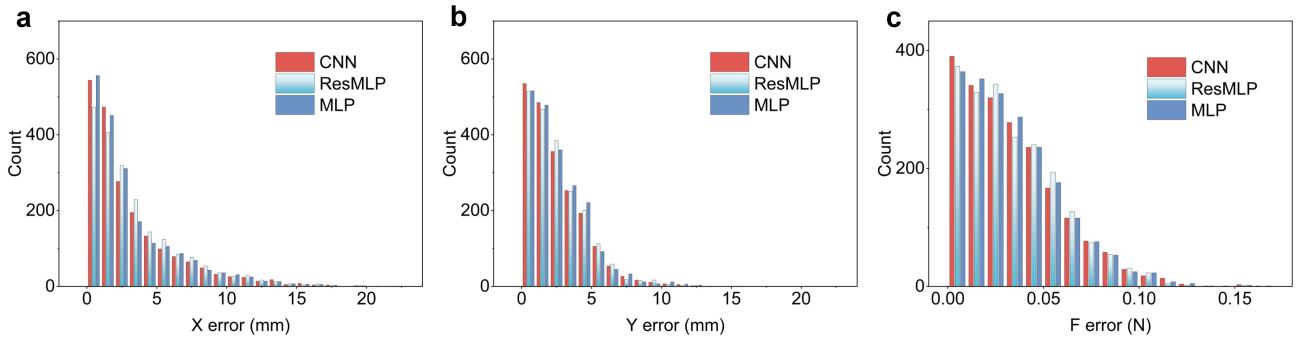


Figure S22. Performance comparison of convolutional neural networks (CNNs), residual multi-layer perceptrons (ResMLPs) and multilayer perceptrons (MLPs). (a) X estimation errors. (b) Y estimation errors. (c) F estimation errors.

Note S7: Comparison Between Three Different Algorithms

The performance comparison of three machine learning algorithms, convolutional neural networks (CNNs), residual multi-layer perceptrons (ResMLPs) and multilayer perceptrons (MLPs) is shown in **Figure** S22. The average location estimation error in the X direction, Y direction, and force estimation error of CNN is 3.183 mm, 2.504 mm and 0.035 N; those for ResMLP are 3.403 mm, 2.541 mm and 0.037 N; and for MLP are 3.190 mm, 2.549 mm and 0.034 N, respectively. The standard deviations (Std) of X estimation error, Y estimation error, and force estimation error of CNN are 3.245 mm, 2.043 mm and 0.026 N; those for ResMLP are 3.178 mm, 2.014 mm and 0.025 N; and for MLP are 3.251 mm, 2.057 mm and 0.025 N, respectively.

These three algorithms can have almost the same performance with fine-tuning; this is mainly because the localization and force estimation problem of the Origami structure is not quite complicated compared with other robotics-related or computer-vision-related problems. Compared with the other two algorithms, the structure of MLP is the most straightforward, and the training cost and computational power required for MLP are also relatively low; this makes it suitable to integrate with the e-skin rather than running outside on an extra PC. This is the reason for implementing MLP in our work.

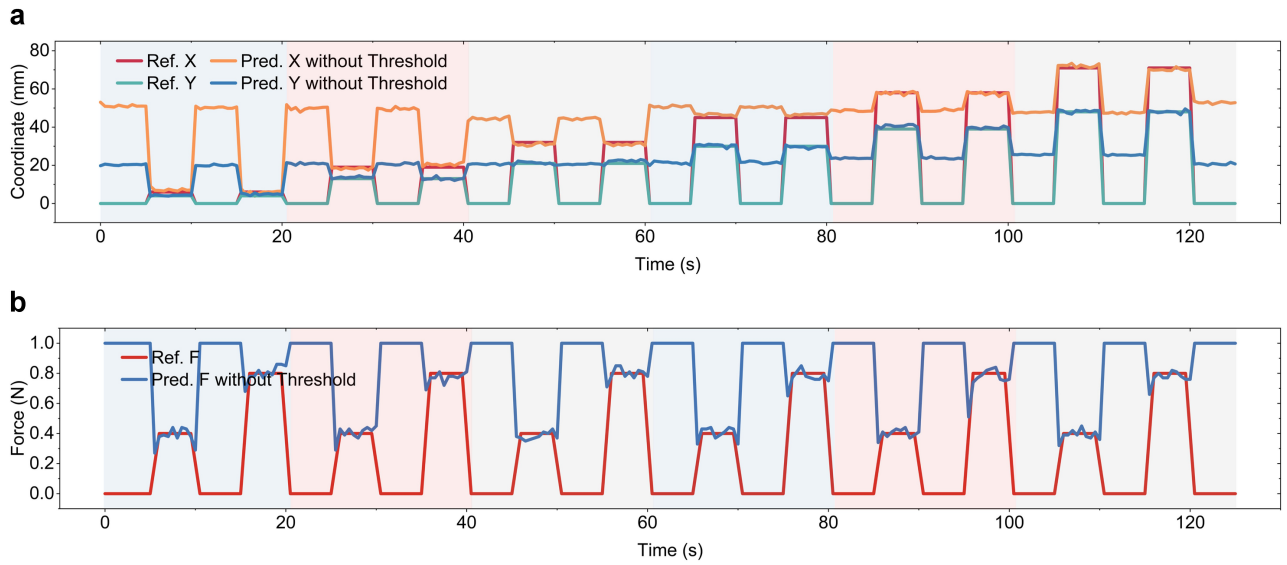


Figure S23. Real-time localization and force estimation without prescribed CDC output threshold. (a) Real-time localization results without threshold. (b) Real-time force estimation results without threshold. When the CDC output threshold is not set, AD7147 still outputs signals under no load due to chip noise fluctuations. Using these data as inputs for machine learning models will lead to inaccurate results.

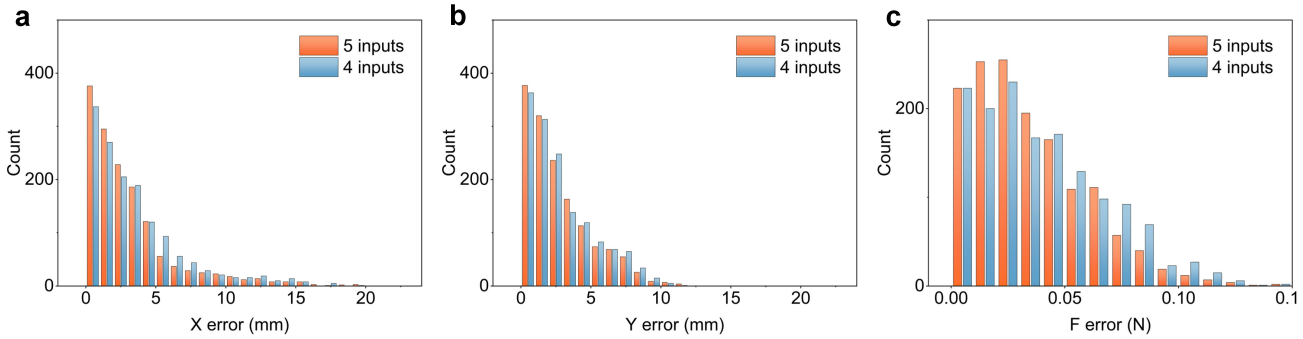


Figure S24. Performance comparison of different inputs (MLPs). 5 inputs: S1, S3, S5, S7, S9 in Figure 4a and 4 inputs: S1, S3, S7, S9. (a) *X* estimation errors for different inputs. (b) *Y* estimation errors for different inputs. (c) *F* estimation errors for different inputs. When the amount of input data for training models decreases, model accuracy may decline. However, for the vast majority of human-machine interaction scenarios, this accuracy remains within a small and usable range. If fabrication precision is further improved to make the structure closer to its ideal state, its deformation transmission capability can be further enhanced, and machine learning accuracy will correspondingly increase. In practical applications, the spacing of sensing units could be determined by balancing the required sensing area, wiring complexity, and precision requirements to achieve an optimal equilibrium across all factors.

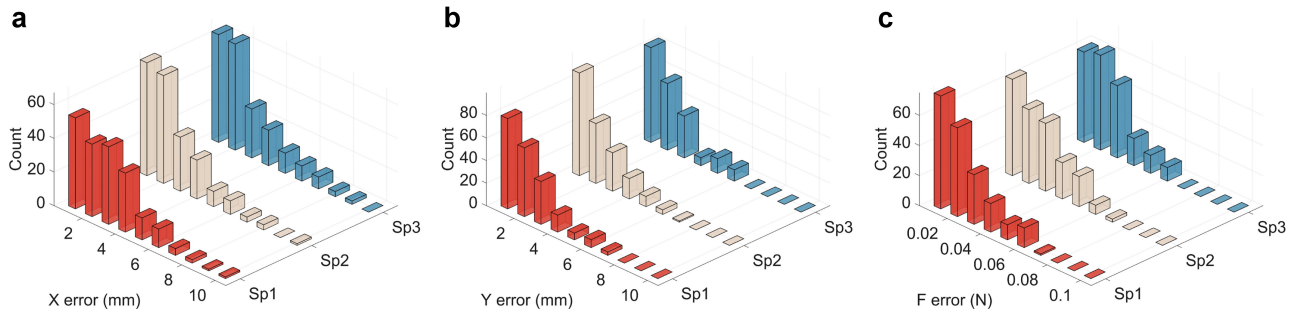


Figure S25. Robustness test of proposed e-skin. Another three curved samples (Sp1, Sp2 and Sp3) were fabricated, and the trained machine learning model from the initial sample was directly used in these three newly fabricated samples. (a) Location estimation performance in *X* direction when directly applying the model trained on one curved sample to another three samples. (b) Location estimation performance in the *Y* direction when directly applying the model trained on one curved sample to the other three samples. (c) Normal load estimation performance in *X* when directly applying the model trained on one curved sample to another three samples. It is obvious with the proposed structure and fabrication process, almost the same performances can be realized even directly use the trained model from one sample to other samples, shows the good robustness of the proposed e-skin.

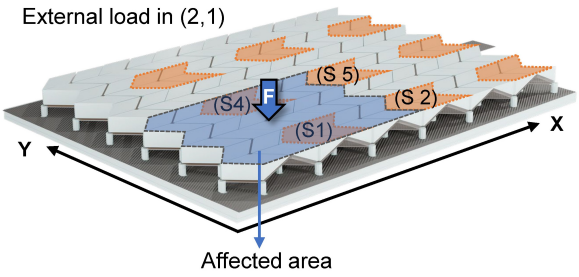


Figure S26. Schematic of proposed e-skin under single external load. Electrodes are highlighted with lighted orange, and the affected area of external load are highlighted in blue.

Note S8: Multi-point Touch Realization Analysis

From the test results, the responsible area of each electrode is defined as its first outer layer of cells, while the affected area of an external load spans a 3×3 region centered on the load. **Figure** S26 shows the schematic under a single-point load. In this scenario, electrodes S1 and S4 exhibit significant variations. The responsible area for S1 includes cells (1,1), (2,1), (3,1), (1,2), (2,2), and (3,2), while that for S4 includes cells (1,2), (2,2), (3,2), (1,3), (2,3), (3,3), (1,4), (2,4), and (3,4). Their overlapping region—cells (1,2), (2,2), and (3,2)—indicates the possible load location. Since S2 and S5 show no significant variation, cell (3,2) can be excluded, and the load is localized near cell (2,2).

Although cell (1,2) could also be a candidate location, this ambiguity (singularity) can be resolved using a 7×7 e-skin with 16 electrodes.If external load is applied on cell (1,2), similar response will also be observed for S1 and S4. In practical applications, only single-load information is typically required, and machine learning algorithms can accurately estimate both load location and magnitude.

Figure S27 illustrates four representative two-point touch scenarios. **Figure** S27a: When the affected areas do not overlap, the two loads can be directly distinguished. For example, S1 and S4 respond to one load while S9 responds to another, allowing both load numbers and approximate locations to be estimated. **Figure** S27b: When the affected areas partially overlap but neither load acts within the other's influence region (and neither is applied on electrodes), the responsible areas of S1, S4, and S7 indicate two loads near cells (2,2) and (2,4). **Figure** S27c: When both loads are applied directly on electrodes (e.g., S4 and S7), only their respective readouts change, and the overlapping area at (2,4) causes the two loads to be recognized as a single equivalent load. **Figure** S27d: When one load is within the affected area of another, only S1 and S4 respond, and the loads are similarly interpreted as one near (2,2).

For cases c and d, although the two external loads cannot be correctly distinguished, distinguishing such loads in practice is unnecessary for most human–machine interaction tasks, as their effects will have no significant differences compared to the equivalent single-point load, where efficient large-area sensing is of greater importance.

Therefore, based on the above analysis, the criteria for determining whether it is a two-point touch are as follows: if only one electrode exhibits a signal change exceeding the threshold (CDC readout variation of 30 here), it is a single-point touch; if two electrodes show signal changes exceeding the threshold (Figure S27c), then examine whether their signal changes conform to the deformation transmission pattern (Figures 4c and d in the manuscript). If they conform, it is a single-point touch; if not, it is a two-point touch. A similar approach applies when more than two electrodes exceed the threshold. Note that when five or more signals exceed the threshold, it is always a two-point touch, as a

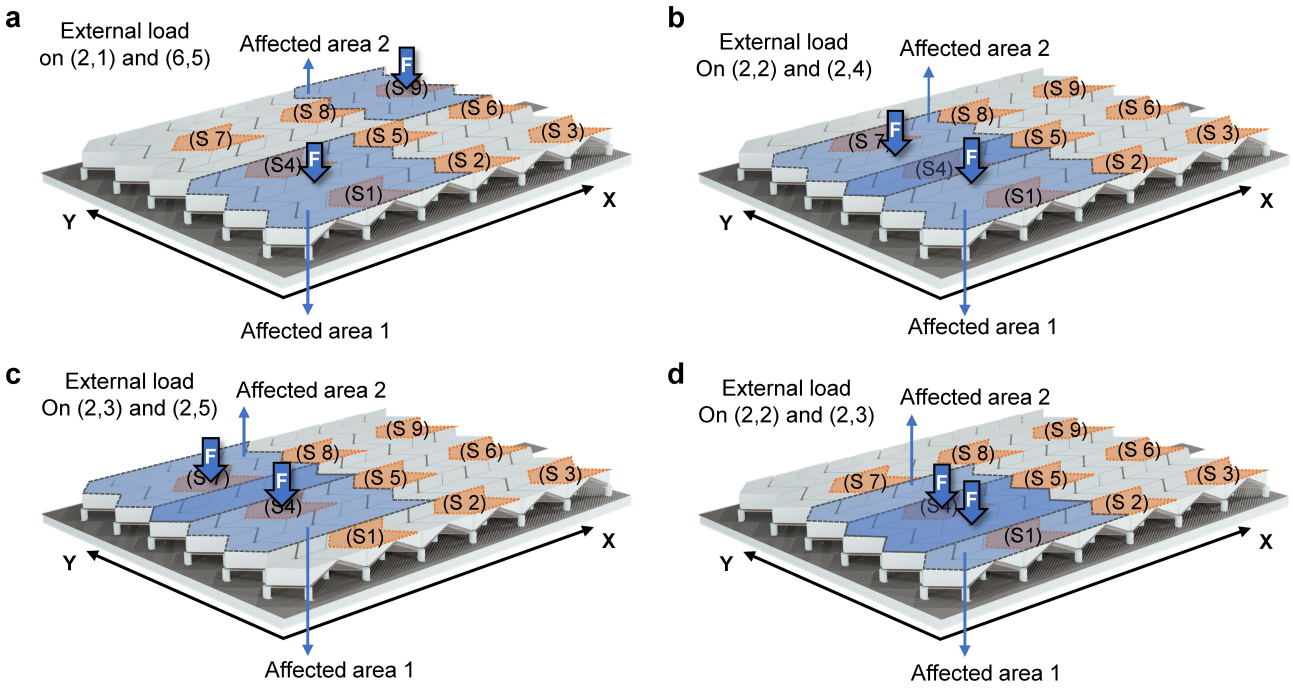


Figure S27. Schematic of proposed e-skin under two external loads. (a) Two external loads applied simultaneously with non-overlapping areas of affect. (b) Two external loads applied simultaneously with overlapping areas of affect, but one load does not act within the area of affect of the other, and both loads are not applied directly on electrodes. (c) Two external loads applied simultaneously with overlapping areas of affect, but one load does not act within the area of affect of the other, and both loads are applied on electrodes. (d) Two external loads applied simultaneously and one load act within the area of affect of the other.

single force can simultaneously cover a maximum of four electrodes.

Then, the tactile sensing process is as follows: based on the output variations of all the electrodes, the number of external loads is determined. Subsequently, depending on the number of external loads, different machine learning models (two-point touch or single-point touch) are called; thus, the locations and magnitudes of external loads can be estimated. This necessitates that the minimum distinguishable distance between two points of force must be two cells or more. In practical applications, since external forces do not always act at the vertices of the origami structure, the minimum distinguishable distance between two points of force using this method is approximately 30 mm.

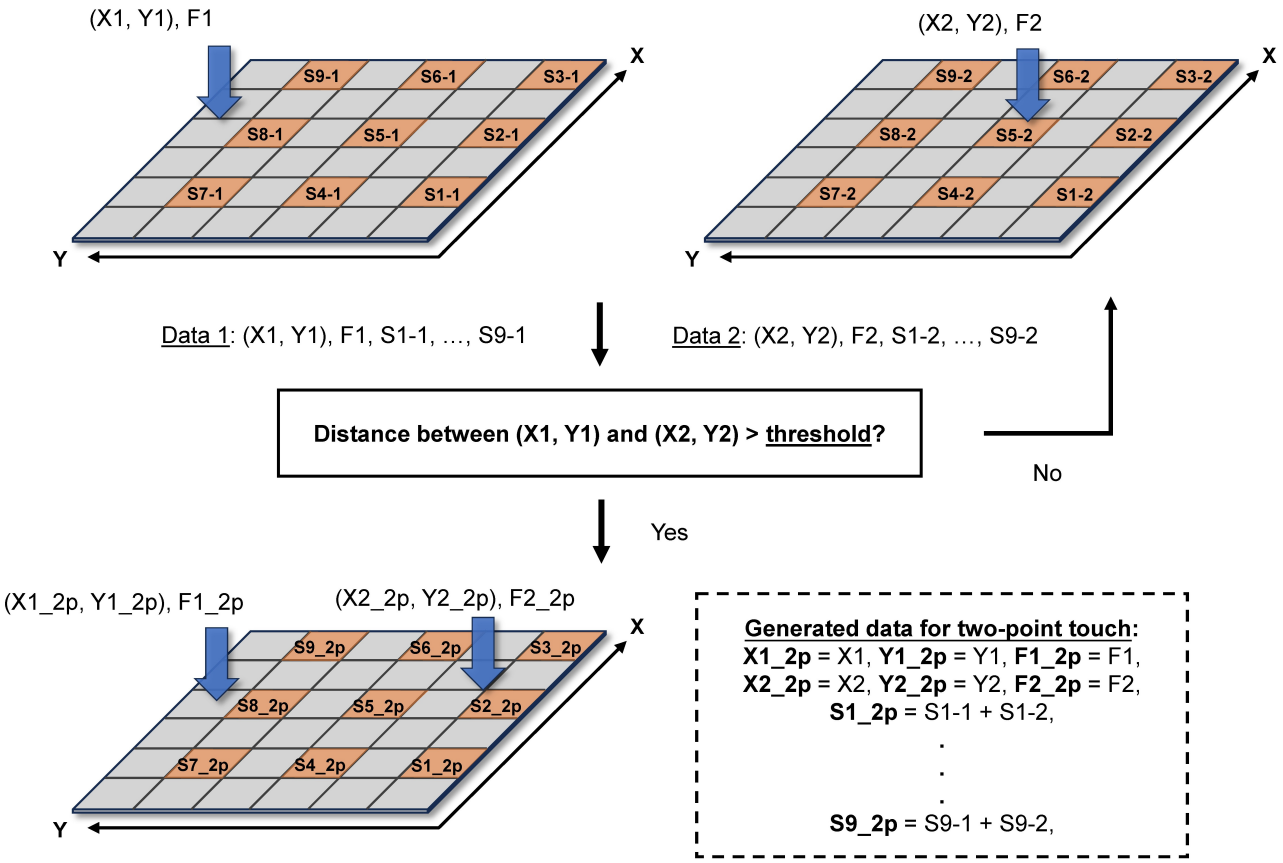


Figure S28. Generation of two-point touch training data. Initially, two different single-point touch data points are selected from the database. The distance between these two points is then calculated and evaluated against a threshold value (if the distance is less than or equal to the threshold, the points are considered adjacent). If the distance exceeds the threshold, the generated two-point touch data represents the direct superposition of the two single-point touch data points (with each electrode corresponding one-to-one). The threshold is set as 30 mm here, according to previous analysis.

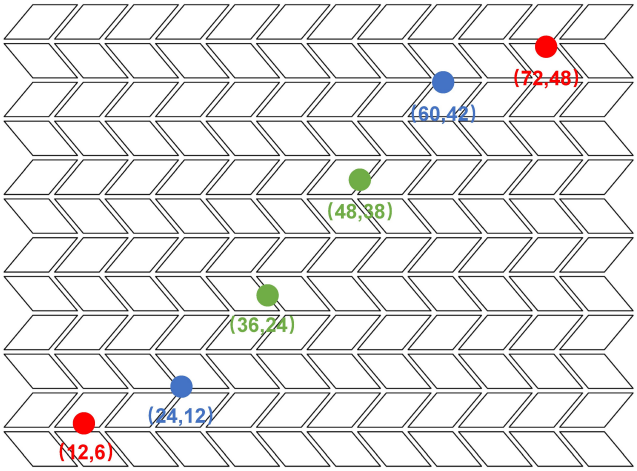


Figure S29. Schematic of tested 6 points for verifying the generated data for two-point touch. Red, green, and blue points are grouped respectively, with each group testing three different combinations of forces. Results are shown in Table S1.

Table S1. Comparison of generated data and collected data for two-point touch. Due to the linearity of the F-CDC curve, there is no significant difference between the data generated by superimposing single-point touch data and the actual measured data within the tested points.

X1	Y1	F1	X2	Y2	F2	Type	S1	S2	S3	S4	S5	S6	S7	S8	S9
12	6	0.4	72	48	0.4	Generated	153	55	117	118	2	23	5	60	106
						Measured	162	47	10	127	7	22	3	56	99
12	6	0.4	72	48	0.8	Generated	148	59	8	103	12	27	10	69	137
						Measured	153	61	2	103	19	23	8	60	132
12	6	0.8	72	48	0.8	Generated	331	60	65	198	75	61	61	53	142
						Measured	333	52	59	189	79	63	54	50	134
24	12	0.4	60	42	0.4	Generated	124	50	32	131	115	26	63	159	85
						Measured	136	59	30	141	115	20	77	148	95
24	12	0.4	60	42	0.8	Generated	128	43	25	149	97	41	65	298	97
						Measured	116	57	25	158	105	41	53	290	111
24	12	0.8	60	42	0.8	Generated	182	83	53	203	152	68	71	313	100
						Measured	178	70	45	192	165	55	74	311	86
36	24	0.4	48	36	0.4	Generated	21	31	14	91	127	75	40	151	42
						Measured	11	15	4	87	127	86	38	145	45
36	24	0.4	48	36	0.8	Generated	28	23	27	85	172	85	51	224	68
						Measured	11	16	18	71	182	87	59	210	59
36	24	0.8	48	36	0.8	Generated	55	51	39	160	268	93	138	242	80
						Measured	65	45	27	158	265	83	120	223	84

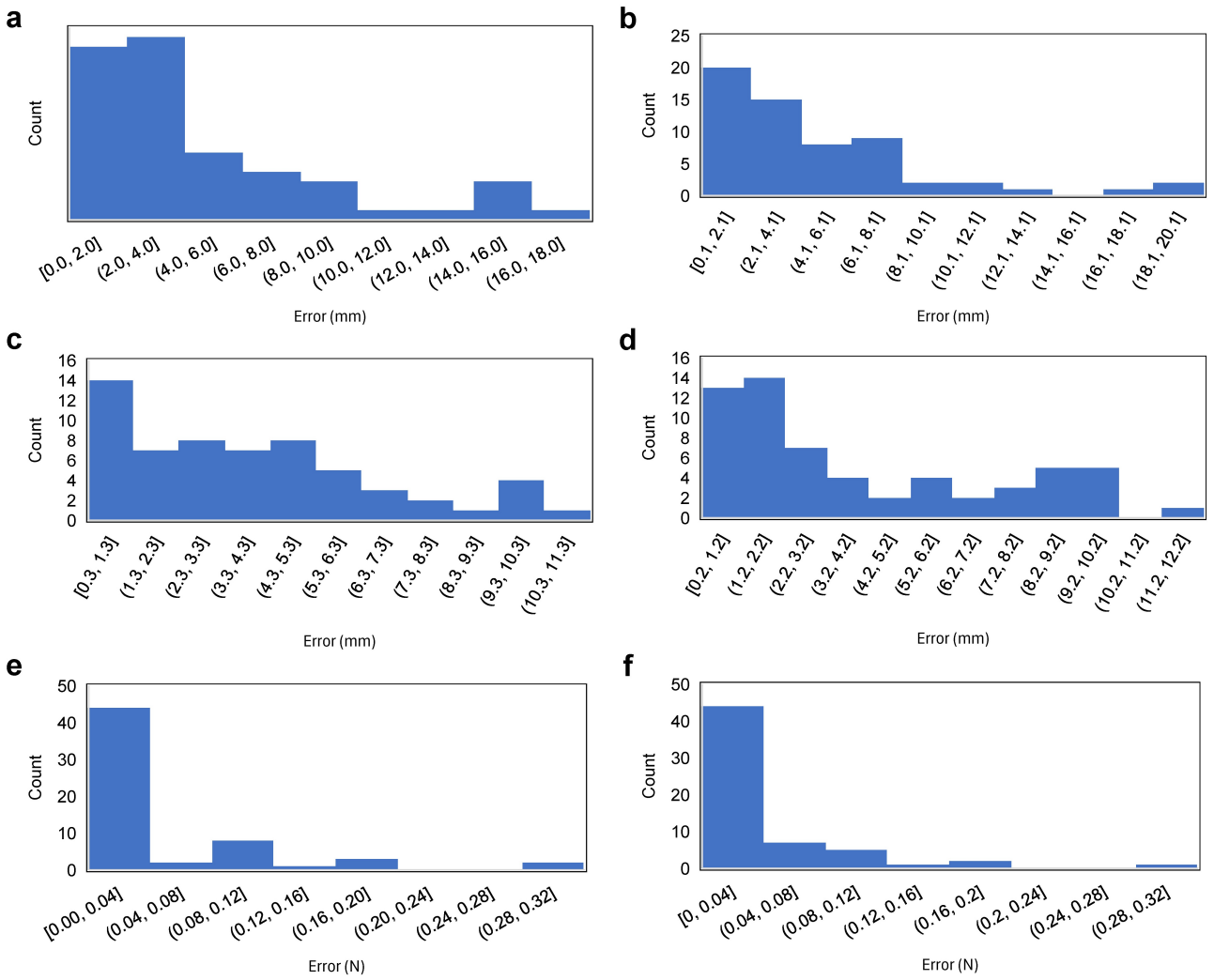


Figure S30. Performance of two-non-adjacent-point touch. In the test, point 1 was selected as six equidistant points along the diagonal, each with two force amplitudes: 0.4 N and 0.8 N. point 2 was assigned a randomly generated position and force by the sliding platform (the position was randomized within the range ensuring successful two-point touch recognition). A total of 60 data sets were collected. (a) X localization error of point 1. Average: 4.5 mm. (b) X localization error of point 2. Average: 4.8 mm. (c) Y localization error of point 1. Average: 3.9 mm. (d) Y localization error of point 2. Average: 3.4 mm. (e) F estimation error of point 1. Average: 0.09 N. (f) F estimation error of point 2. Average: 0.07 N.

References

S1. Sun, H. & Martius, G. Guiding the design of superresolution tactile skins with taxel value isolines theory. *Sci. Robotics* **7**, eabm0608 (2022).

S2. Callens, S. J. & Zadpoor, A. A. From flat sheets to curved geometries: Origami and kirigami approaches. *Mater. Today* **21**, 241–264 (2018).

S3. Dudte, L. H., Vouga, E., Tachi, T. & Mahadevan, L. Programming curvature using origami tessellations. *Nat. materials* **15**, 583–588 (2016).

S4. Gattas, J. M., Wu, W. & You, Z. Miura-base rigid origami: parameterizations of first-level derivative and piecewise geometries. *J. Mech. design* **135**, 111011 (2013).

S5. Deng, Y. *et al.* Curved display based on programming origami tessellations. *Microsystems & Nanoeng.* **7**, 101 (2021).

S6. Holzapfel, G. A. Nonlinear solid mechanics: a continuum approach for engineering science (2002).

S7. Guggenheimer, H. W. *Differential geometry* (Courier Corporation, 2012).